Biophysical Journal Volume 109 December 2015 2246–2258

Article

An Intermittent Model for Intracellular Motions of Gold Nanostars by k-Space Scattering Image Correlation

Margaux Bouzin,[1] Laura Sironi,[1] Giuseppe Chirico,[1] Laura D'Alfonso,[1] Donato Inverso,[2] Piersandro Pallavicini,[3] and Maddalena Collini[1,*]

[1]Physics Department, Università degli Studi di Milano-Bicocca, Milan, Italy; [2]Division of Immunology, Transplantation and Infectious Diseases, IRCCS, San Raffaele Scientific Institute, Milan, Italy; and [3]Chemistry Department, Università degli Studi di Pavia, Pavia, Italy

ABSTRACT Anisotropic metallic nanoparticles have been devised as powerful potential tools for in vivo imaging, photothermal therapy, and drug delivery thanks to plasmon-enhanced absorption and scattering cross sections, ease in synthesis and functionalization, and controlled cytotoxicity. The rational design of all these applications requires the characterization of the nanoparticles intracellular trafficking pathways. In this work, we exploit live-cell time-lapse confocal reflectance microscopy and image correlation in both direct and reciprocal space to investigate the intracellular transport of branched gold nanostars (GNSs). Different transport mechanisms, spanning from pure Brownian diffusion to (sub-)ballistic superdiffusion, are revealed by temporal and spatio-temporal image correlation spectroscopy on the tens-of-seconds timescale. According to these findings, combined with numerical simulations and with a Bayesian (hidden Markov model-based) analysis of single particle tracking data, we ascribe the superdiffusive, subballistic behavior characterizing the GNSs dynamics to a two-state switching between Brownian diffusion in the cytoplasm and molecular motor-mediated active transport. For the investigation of intermittent-type transport phenomena, we derive an analytical theoretical framework for Fourier-space image correlation spectroscopy (kICS). At first, we evaluate the influence of all the dynamic and kinetic parameters (the diffusion coefficient, the drift velocity, and the transition rates between the diffusive and the active transport regimes) on simulated kICS correlation functions. Then we outline a protocol for data analysis and employ it to derive whole-cell maps for each parameter underlying the GNSs intracellular dynamics. Capable of identifying even simpler transport phenomena, whether purely diffusive or ballistic, our intermittent kICS approach allows an exhaustive investigation of the dynamics of GNSs and biological macromolecules.

INTRODUCTION

The capability of converting the absorbed energy into heat via nonradiative electron relaxation dynamics and of inducing localized heating effects (1,2) makes gold nanoparticles (GNPs) widely employed for cancer cell photothermal treatments (3–5) or as nanocarriers that can thermally release loaded molecules (6,7). GNPs of asymmetric shapes, such as rods, stars, cages, and shells (8–10), are particularly indicated for photothermal treatments because their major plasmon resonance absorption band falls in the near-infrared region of the electromagnetic spectrum (680–900 nm) and is fine-tunable during the synthesis (1,11–14). This same absorption band also confers to asymmetric GNPs a large luminescence signal upon two-photon excitation in the infrared peak, thereby creating an intrinsic optical tool to detect them in living systems (14–16). However, a two-photon setup is not always available in most laboratories, where a scanning confocal microscope exploiting visible laser lines is usually present. Nanoparticles labeling with fluorescent dyes can lead to the dye release in the cytoplasm or in the acidic environment of lysosomes and endosomes, and may alter the NPs surface charge and aggregation state. Alternative methods for the label-free detection of NPs in living cells are therefore desirable.

Cells can uptake NPs by means of very different mechanisms depending upon their size, charge, surface coating, and shape (17–19). To develop nanodevices that can target cell organelles or act on specific cell metabolic paths, it is critical to know how the internalization process occurs and how the GNPs behave once they are inside the cytoplasm. No unique model has been devised for the intracellular transport of nanoparticles and, more in general, of organelles, vesicles, and cargoes: experimental results reported in the literature vary from Brownian motion (20,21) to anomalous super- (21–23) and subdiffusion (24,25), the latter usually being described with the aid of approximate, effective models (24,26). While subdiffusion is usually attributed to elastic trapping, obstructions, meshworklike domains, and stalling (23), it is largely accepted that superdiffusion is due to the collective action of dynein, kinesin, and myosin molecular motors, responsible for the intracellular active transport of cargoes along the semiflexible oriented filaments of the cytoskeleton (27–31). The overall mobility of these cargoes as they randomly bind and unbind to motor proteins is a complex interplay of free thermal diffusion in the cytoplasm and directed,

Submitted August 3, 2015, and accepted for publication October 21, 2015.

*Correspondence: maddalena.collini@mib.infn.it

Editor: Paul Wiseman.

0006-3495/15/12/2246/13

http://dx.doi.org/10.1016/j.bpj.2015.10.025

ballistic displacements along actin filaments and microtubules (32). Overall, due to the heterogeneity of the cytoplasmic environment and to the resulting variability of intracellular transport mechanisms, it would be very useful to derive a model-free analysis protocol capable of quantitatively characterizing the mode of motion without any prior assumption on its Brownian or superdiffusive nature.

In this work, we employ live-cell confocal time-lapse imaging and the detection of the scattering signal of branched gold nanostars (GNSs) to follow their dynamics upon internalization in cellular (endocytotic) vesicles. By the temporal and spatial correlation of the acquired *xyt* stacks, we quantify the characteristic timescale of the vesicles dynamics and identify the presence of different transport processes spanning from pure to enhanced diffusion. We combine the idea of intermittent dynamics usually exploited to model search and target-finding processes (33,34) with the traditional formalism adopted for the description of chemical reactions in point fluorescence correlation spectroscopy (FCS) (35,36), to propose an intermittent model to be applied through k-space image correlation spectroscopy (kICS). By involving the switch between a passive and an active diffusional state, our model identifies the simplest stochastic transport model that accurately describes the experimental data and allows us to map the dynamic and kinetic parameters governing the GNSs intracellular (active) transport. The results are finally corroborated by a Bayesian analysis of single particle tracking data providing a parallel estimate of the equilibrium probabilities of the two states.

MATERIALS AND METHODS

Methods

Temporal image correlation spectroscopy

Temporal image correlation spectroscopy (TICS) (37,38) has been conceived as the imaging analog of FCS (39,40). Given an *xyt* stack of raster-scanned images, TICS relies on the computation, for each lag time τ, of the temporal autocorrelation function (ACF) as

$$G(\tau) = \frac{\langle \delta I(x,y,t)\delta I(x,y,t+\tau)\rangle_t}{\langle I(x,y,t)\rangle_t^2}. \quad (1)$$

In Eq. 1 the intensity fluctuations are defined as $\delta I(x,y,t) = I(x,y,t) - \langle I(x,y,t)\rangle_t$, where $I(x,y,t)$ is the intensity recorded at image pixel position (x,y) at time t and the angular brackets denote a temporal average over the entire pixel time series. The subtraction of $\langle I(x,y,t)\rangle_t$ acts as an immobile population removal.

For the simple case of 2D Brownian diffusion, sampled by a TEM_{00} laser beam with Gaussian radial intensity profile, Eq. 1 can be analytically derived (38,41), leading to a hyperbolic decay with characteristic relaxation time τ_d:

$$G(\tau) = G(0)\left(1+\frac{\tau}{\tau_d}\right)^{-1} + G_\infty. \quad (2)$$

For confocal detection schemes $\tau_d = \omega_0^2/(4D)$, where ω_0 is the excitation laser beam waist, D is the diffusion coefficient of the investigated objects and G_∞ is an offset accounting for the computation of the experimental correlation function on a finite dataset (42,43). If diffusion is superimposed to a drift with velocity $\underline{v}$, the hyperbolic correlation function is modulated by an exponential factor (41) decaying on a characteristic time $\tau_v = \omega_0/|\underline{v}|$:

$$G(\tau) = G(0)\left(1+\frac{\tau}{\tau_d}\right)^{-1} \times \exp\left[-\left(\frac{\tau}{\tau_v}\right)^2\left(1+\frac{\tau}{\tau_d}\right)^{-1}\right] + G_\infty. \quad (3)$$

By linear combinations of Eqs. 2 and 3, the explicit expression of the temporal ACF for multiple populations undergoing drift and/or Brownian diffusion can be readily obtained (41). We remark that, due to the dependence of Eq. 3 on the modulus $|\underline{v}|$ of the drift velocity, TICS is insensitive to the direction in which the particles exit the correlation volume.

Spatio-temporal image correlation spectroscopy

Spatio-temporal image correlation spectroscopy (STICS) is particularly useful when directed motions are present, due to its sensitivity to both the modulus and the direction of the drift velocity, and has been previously described for the investigation of simple transport phenomena (41,44,45). Briefly, given an *xyt* stack of raster-scanned confocal images, a generalized spatio-temporal correlation function (STCF) is defined, for a lag time τ and for spatial lag variables ξ and η, as

$$G(\xi,\eta,\tau) = \left\langle \frac{\langle \delta i(x,y,t)\delta i(x+\xi,y+\eta,t+\tau)\rangle_{x,y}}{\langle i(x,y,t)\rangle_{x,y}\langle i(x,y,t+\tau)\rangle_{x,y}} \right\rangle_t, \quad (4)$$

where $i(x,y,t)$ defines a corrected pixel intensity, which is obtained by subtracting to the detected value $I(x,y,t)$ the average intensity $\langle I(x,y,t)\rangle_t$ of the pixel time trace (to eliminate the contribution of the immobile population (44), as in TICS) and by subsequently adding the average intensity of the entire *xyt* stack (to avoid oscillatory, noisy correlation functions due to spatially averaged image intensities close to zero (46)). Spatially averaged corrected intensities of the entire *xy* images—or of the selected region of interest (ROI) on which the STICS analysis is performed—at time t and time $t+\tau$ in the temporal series, appearing in the denominator of Eq. 4, are exploited for the computation of corrected intensity fluctuations as $\delta i(x,y,t) = i(x,y,t) - \langle i(x,y,t)\rangle_{x,y}$.

As for TICS, the analytical expression of Eq. 4 has been derived for the simple case of Brownian diffusion and for diffusive motions coupled to directional flow (47):

$$G(\xi,\eta,\tau) \propto \frac{1}{\omega_0^2 + 4D(\xi\tau_p + \eta\tau_l + \tau)} \times \exp\left\{-\frac{|\xi\delta x - v_x(\xi\tau_p + \eta\tau_l + \tau)|^2}{\omega_0^2 + 4D(\xi\tau_p + \eta\tau_l + \tau)}\right\} \times \exp\left\{-\frac{|\eta\delta x - v_y(\xi\tau_p + \eta\tau_l + \tau)|^2}{\omega_0^2 + 4D(\xi\tau_p + \eta\tau_l + \tau)}\right\}. \quad (5)$$

Here δx is the pixel size, and v_x, v_y are the x- and y components of the drift velocity. The values τ_p and τ_l define the pixel dwell time and the line scan time, respectively. Under our typical experimental conditions, $\xi\tau_p + \eta\tau_l + \tau \cong \tau$ and, for a fixed lag time, Eq. 5 can be approximated by a 2D Gaussian. The variance increases linearly with the lag time; D can therefore be recovered either by surface fitting the experimental 2D correlation functions to Eq. 5, or by the linear regression of the variance-versus-τ plot. The peak value is located at $(\xi_{max}, \eta_{max})\delta x = (0,0)$ if $(v_x,v_y) = (0,0)$, whereas it

shifts at $(\xi_{max}, \eta_{max})\delta x \cong (v_x\tau, v_y\tau)$ when $|\underline{v}| \neq 0$; this allows us to measure the x- and y components of the drift velocity by simply tracking the Gaussian peak coordinates (ξ_{max}, η_{max}) as a function of τ (41,44).

Image correlation for intermittent active transport: STICS and kICS

Attempts have been made in deriving the analytical expression of Eqs. 1 and 4 for more complex transport phenomena, resulting from the binding/unbinding of fluorescently labeled macromolecules to immobile cellular substrates or to unlabeled diffusing receptors in the plasma membrane. In the first case, the particle motion occurs intermittently, with phases of Brownian diffusion alternating with periods of immobility. The theoretical framework, which has been derived for point-FCS (48), can be readily extended to the TICS analysis. The second case, where the overall transport can be modeled by two diffusive states characterized by different diffusion coefficients, has been treated (49) for kICS (50,51).

As suggested by our experimental results, we derive here the theoretical framework—for both STICS and its k-space version kICS—for a third type of intermittent transport that best describes the switching between phases of thermal diffusion and phases of active transport mediated by molecular motors inside living cells. Previous derivations for particle image correlation spectroscopy (52,53) require numerical data fitting. We find here, instead, an analytical solution to the problem that can be readily employed for experimental data analysis.

Hence we consider a particle freely diffusing in a 2D-dimensional space (20,29) that randomly binds to molecular motor proteins. Under the simplifying assumption of an effective unimolecular reaction (48) and by denoting with k_{12} and k_{21} the association and dissociation rates, respectively, a two-state system of the form

$$D \underset{k_{21}}{\overset{k_{12}}{\rightleftarrows}} D + \underline{v} \tag{6}$$

can be considered, where states (1) and (2) are identified by the mode of motion exhibited by the particle (respectively, Brownian diffusion and diffusive active transport with constant velocity $\underline{v} = (v_x, v_y)$). We do not take into account possible changes in the diffusion coefficient D due to the switching between states (1) and (2), to minimize the employed number of model parameters. This assumption appears to be sufficient to describe the experimental data (see Results and Discussion).

If we call $\delta C_{i\,=\,1,2}(\underline{r},t)$, the fluctuation in the local particle concentration in state (i), the differential equations describing the two-state system above can be written as (39)

$$\begin{cases} \dfrac{\partial}{\partial t}\delta C_1(\underline{r},t) = D\nabla^2\delta C_1(\underline{r},t) - k_{12}\delta C_1(\underline{r},t) + k_{21}\delta C_2(\underline{r},t) \\ \dfrac{\partial}{\partial t}\delta C_2(\underline{r},t) = D\nabla^2\delta C_2(\underline{r},t) - \underline{v}\cdot\nabla\left(\delta C_2(\underline{r},t)\right) \\ \qquad\qquad -k_{21}\delta C_2(\underline{r},t) + k_{12}\delta C_1(\underline{r},t) \end{cases} . \tag{7}$$

The expressions in Eq. 7 are conveniently solved in Fourier space (54), leading to the general solutions for $\delta\widehat{C}_1(\underline{k},t)$ and $\delta\widehat{C}_2(\underline{k},t)$ in terms of the initial conditions $\delta\widehat{C}_1(\underline{k},0)$ and $\delta\widehat{C}_2(\underline{k},0)$. These are subsequently employed in the derivation of the 2D spatio-temporal correlation function of Eq. 4. The calculation, reported in detail in Note S1 of the Supporting Material, yields

$$G(\xi,\eta,\tau) \equiv G(\Delta,\tau) \propto \int d\underline{k} G(\underline{k},\tau)\exp(-i\underline{k}\cdot\underline{\Delta}), \tag{8}$$

where the 2D vector $\underline{\Delta}$ has been introduced to identify the spatial lags $(\xi,\eta)\,\delta x$; the value $G(\underline{k},\tau)$ is given by

$$G(\underline{k},\tau) \propto \left|\widehat{W}(\underline{k})\right|^2 \frac{1}{k_{12}+k_{21}} \frac{1}{\lambda^{(1)}-\lambda^{(2)}} \left\{A\exp\left[\lambda^{(1)}\tau\right] + B\exp\left[\lambda^{(2)}\tau\right]\right\} \tag{9}$$

with

$$\begin{cases} \lambda^{(1)} = \dfrac{-2D|\underline{k}|^2 - (k_{12}+k_{21}) + i\underline{k}\cdot\underline{v} + \sqrt{\Lambda}}{2} \\ \lambda^{(2)} = \dfrac{-2D|\underline{k}|^2 - (k_{12}+k_{21}) + i\underline{k}\cdot\underline{v} - \sqrt{\Lambda}}{2} \\ \Lambda = (k_{12}+k_{21})^2 - |\underline{k}\cdot\underline{v}|^2 + 2i\underline{k}\cdot\underline{v}(k_{12}-k_{21}) \end{cases} \tag{10a}$$

and

$$\begin{cases} A = k_{12}k_{21} + k_{12}\left(\lambda^{(1)}+\psi\right) - k_{21}\left(\lambda^{(2)}+\psi\right) \\ \qquad -\left(\lambda^{(1)}+\psi\right)\left(\lambda^{(2)}+\psi\right) \\ B = -k_{12}k_{21} - k_{12}\left(\lambda^{(2)}+\psi\right) + k_{21}\left(\lambda^{(1)}+\psi\right) \\ \qquad +\left(\lambda^{(1)}+\psi\right)\left(\lambda^{(2)}+\psi\right) \\ \psi = D|\underline{k}|^2 + k_{12}. \end{cases} \tag{10b}$$

Here, $\widehat{W}(\underline{k})$ in Eq. 9 is the Fourier transform of the excitation beam profile, that, for one photon excitation, we model as a 2D Gaussian with amplitude W_0 and e^{-2} radial beam waist ω_0 (55):

$$\widehat{W}(\underline{k}) = \frac{W_0\omega_0^2}{4}\exp\left\{-\frac{\omega_0^2|\underline{k}|^2}{8}\right\}. \tag{11}$$

Equations 8–11 provide the full STICS theoretical framework for the investigation of intermittent active transport. Although no analytical solution can be provided for the integral in Eq. 8, all the dynamic and kinetic parameters (D, $\underline{v}$, k_{12}, and k_{21}) could in principle be recovered by a nonlinear least-squares numerical fit in the complex field of experimental correlation functions.

A convenient alternative, having the main advantage of not requiring the numerical integration of Eq. 8, is offered by the Fourier-space version of STICS, namely kICS (50,51). The kICS correlation function (hereafter referred to as $G(\underline{k},\tau)$) can be computed as the Fourier transform of the STICS correlation function $G(\underline{\Delta},\tau)$, or equivalently by the spatio-temporal correlation of the Fourier transform of the experimental xyt stack employed for the TICS and STICS analyses. Because Eq. 8 relates the spatio-temporal correlation functions in the direct and reciprocal spaces, the kICS formalism is directly provided by Eqs. 9–11. We note that $G(\underline{k},\tau)$ is defined in the complex space, but the analytical separation of its real and imaginary parts is prevented.

In the limit $k_{12}\to+\infty$ and $k_{21}\to 0$, Eq. 9 reduces (see the Supporting Material) to the simpler expression

$$G(\underline{k},\tau) = \left|\widehat{W}(\underline{k})\right|^2\exp\left(-D|\underline{k}|^2\tau + i\underline{k}\cdot\underline{v}\tau\right), \tag{12}$$

which, in agreement with the literature (49,50), describes the case of Brownian diffusion and uniform drift $\underline{v}$.

In the Supporting Material, the derivation of the kICS correlation function is also extended to the more general case of intermittent 3D active transport, though no analytical solution can be derived.

Single particle tracking

An alternative method to analyze intracellular transport is single particle tracking (SPT) (56–58). This well-established technique is based on the computation of the trajectory, i.e., the sequence of positions $\underline{r}(t_j)$ at times

$t_{j=1...N}$, of individual (fluorescent or scattering) mobile particles imaged in time-lapse mode.

Mean-square displacement analysis. The particle coordinates $(x(t_j), y(t_j)) = \underline{r}(t_j)$, determined with ~10 nm accuracy by centroid calculations (56,59), are typically exploited in the computation of the mean-square displacement (56,60,61) MSD($n\Delta t$), where $n\Delta t$ is an integer multiple of the temporal separation Δt between consecutively sampled points in the trajectory. In Eq. 13, we report the MSD explicit expressions for the three transport phenomena we have considered in the previous paragraphs: 1) Brownian diffusion, which results in a linear MSD-versus-τ plot (56–62); 2) the coupling of thermal diffusion and uniform drift, which endows the MSD plot with positive curvature (56–62); and 3) the intermittent active transport described by Eq. 6, for which the MSD depends on the diffusion coefficient and the drift velocity as well as on the jump rates between the two states.

$$\begin{cases} (i)MSD(\tau) = 4D\tau \\ (ii)MSD(\tau) = 4D\tau + |\underline{v}|^2\tau^2 \\ (iii)MSD(\tau) = 4D\tau + |\underline{v}|^2_{\text{eff}}\tau^2 + 2\tau_{\text{rel}}\dfrac{k_{21}}{k_{12}}|\underline{v}|^2_{\text{eff}} \\ \qquad\qquad \times \left[\tau - \tau_{\text{rel}}\left(1 - e^{-\tau/\tau_{\text{rel}}}\right)\right] \end{cases} \tag{13}$$

We derived Eq. 13(*iii*) by extending the treatment reported in Berezhkovskii and Bezrukov (63) to a 2D motion in the xy plane. $\tau_{\text{rel}} = (k_{12}+k_{21})^{-1}$ is the system relaxation time and $|\underline{v}|_{\text{eff}} = |\underline{v}|k_{12}/(k_{12} + k_{21})$ is an effective drift speed weighted for the equilibrium probability p_2^{eq} of finding the particle in state (*ii*), defined as

$$\begin{aligned} p_2^{\text{eq}} &= k_{12}/(k_{12} + k_{21}); \\ p_1^{\text{eq}} &= 1 - p_2^{\text{eq}} = k_{21}/(k_{12} + k_{21}). \end{aligned} \tag{14}$$

Experimentally, a constant term is usually added to the expressions in Eq. 13(*i–iii*) to account for the uncertainty on the particle localization (62,64).

Bayesian-based analysis of single particle tracks. A second promising approach for the analysis of SPT data has been proposed recently, involving the application of hidden Markov models to the particle tracking analysis (65–67). Each trajectory is regarded as the outcome of an m-state Markov chain, with the ith state, $i = 1...m$, parameterized by a diffusion coefficient D_i and a drift velocity $\underline{v}_i$. At each time point $t_{j=1...N}$, the particle state determines the length and direction of the next displacement $\Delta\underline{r}(t_{j+1}) = \underline{r}(t_{j+1}) - \underline{r}(t_j)$: therefore, although the N-step state sequence $\mathbf{s}$ underlying the trajectory (and hence the exact state the particle occupies at time t_j) is unknown (hidden), the experimental measurement of all the particle displacements assigned by $\mathbf{s}$ allows inferring information on the sequence $\mathbf{s}$ itself, as well as on the diffusion coefficients and drift velocities of the constituent states and on the rates of transition between them. To this aim we adopted the likelihood maximization strategy summarized in the following.

Let $\theta = \{D_{i=1...m}, \underline{v}_{i=1...m}, p_{i,j=1...m}\}$ be the set of unknown parameters for a d-dimensional trajectory described by an m-state Markov chain. For $d = 2$ (2D tracking experiment) and $m = 2$ (as in Eq. 6), the transition probabilities $p_{i,j=1,2}$ per time step (Δt) are related to the rate constants k_{12} and k_{21} by

$$\begin{cases} p_{12} = \dfrac{k_{12}}{k_{12} + k_{21}}\{1 - \exp[-(k_{12} + k_{21})\Delta t]\} \\ p_{21} = \dfrac{k_{21}}{k_{12} + k_{21}}\{1 - \exp[-(k_{12} + k_{21})\Delta t]\} \\ p_{11} = 1 - p_{12} \\ p_{22} = 1 - p_{21}. \end{cases} \tag{15}$$

The set of independent parameters reduces in this case to $\theta = \{D_{i=1,2}, |\underline{v}_{i=1,2}|, \alpha_{i=1,2}, p_{12}, p_{21}\}$, where α_i is the angle defining the x- and y components of the drift velocity vector $\underline{v}_i$ ($v_{xi} = |\underline{v}_i|\cos(\alpha_i)$, $v_{yi} = |\underline{v}_i|\sin(\alpha_i)$). According to Bayes' theorem, assuming a uniform prior probability $p(\theta)$ and marginalizing the likelihood over all possible hidden state sequences $\mathbf{s}$, the likelihood of a parameters set θ given an experimental trajectory $\underline{r}(t_{j=1...N})$ can be written as

$$\begin{aligned} \ell(\theta|\underline{r}(t_1), \underline{r}(t_2), \ldots, \underline{r}(t_N)) &\propto p(\underline{r}(t_1), \underline{r}(t_2), \ldots, \underline{r}(t_N)|\theta) \\ &= \sum p(\underline{r}(t_1), \underline{r}(t_2), \ldots, \underline{r}(t_N)|s, \theta)p(s|\theta). \end{aligned} \tag{16}$$

The summation over state sequences can be performed efficiently by the forward-backward algorithm (65,68). It allows computing the logarithm of the right-hand side of Eq. 16, leading to

$$\ln[\ell(\theta|\underline{r}(t_1), \underline{r}(t_2), \ldots, \underline{r}(t_n))] \propto \ln\left(e^{\phi_1(N)} + e^{\phi_2(N)}\right), \tag{17}$$

where the ϕ-terms are defined recursively according to

$$\begin{cases} \phi_i(j) = \ln\left(e^{\phi_1(j-1)+log(p_{1i})} + e^{\phi_2(j-1)+log(p_{2i})}\right) \\ \qquad\quad +\ln\left[\ell\left(D_i, |\underline{v}_i|, \alpha_i|\underline{\Delta r}(t_j)\right)\right] \\ \phi_i(1) = \ln(p_i^{\text{eq}}) + \ln[\ell(D_i, |\underline{v}_i|, \alpha_i|\underline{\Delta r}(t_1))]. \end{cases} \begin{cases} i = 1, 2 \\ j = 2...N \end{cases} \tag{18}$$

Equilibrium probabilities in Eq. 18 obey the previous definition (Eq. 14), while $\ell(D_i, |\underline{v}_i|, \alpha_i|\underline{\Delta r}(t_j))$—the likelihood of the dynamic parameters D_i, $|\underline{v}_i|$, α_i given the individual displacement $\underline{\Delta r}(t_j)$—is computed (and inserted into Eq. 18) from Bayes' rule: it is proportional to the normal distribution with variance $4D_i\Delta t$ and mean $\underline{v}_i\Delta t$ defining the probability density of observing a displacement $\underline{\Delta r}(t_j)$ in a time interval $\Delta t = t_j - t_{j-1}$ given that the particle is in state (i) at time t_j (56,69). Hence,

$$\begin{cases} \ell\left(D_i, |\underline{v}_i|, \alpha_i|\underline{\Delta r}(t_j)\right) \equiv \ell\left(D_i, \underline{v}_i|\underline{\Delta r}(t_j)\right) \propto P\left(\underline{\Delta r}(t_j)|D_i, \underline{v}_i\right) \\ P\left(\underline{\Delta r}(t_j)|D_i, \underline{v}_i\right) = \dfrac{1}{4\pi D_i\Delta t}\exp\left\{-\dfrac{|\underline{\Delta r}(t_j) - \underline{v}_i\Delta t|^2}{4D_i\Delta t}\right\} \\ = \dfrac{1}{4\pi D_i\Delta t}\exp\left\{-\dfrac{|\Delta x(t_j) - v_{xi}\Delta t|^2 + |\Delta y(t_j) - v_{yi}\Delta t|^2}{4D_i\Delta t}\right\}. \end{cases} \tag{19}$$

The log-likelihood computed through Eqs. 17–19 must then be maximized with respect to θ to retrieve the most probable set of model parameters, hereafter referred to as Θ:

$$\begin{aligned} \Theta &= \underset{\theta}{\text{argmax}}\{\ln[\sum p(\underline{r}(t_1), \underline{r}(t_2), \ldots, \underline{r}(t_N)|s, \theta)p(s|\theta)]\} \\ &= \underset{\theta}{\text{argmax}}\left\{\ln\left(e^{\phi_1(N)} + e^{\phi_2(N)}\right)\right\}. \end{aligned} \tag{20}$$

We perform this maximization by a Markov chain Monte Carlo (MCMC) (70) algorithm, as described in Note S2 in the Supporting Material.

Materials

Gold nanostars synthesis

GNSs have been synthesized by a LSB (laurylsulphobetaine)-driven seed-mediated growth as described elsewhere (13,71) ([LSB] = 0.35 M). As

derived from transmission electron microscopy images, the GNSs have average branch sizes of (53 ± 12) nm and (9 ± 2) nm, yielding a plasmonic absorption band centered at 780 nm. The diffusion coefficient of GNSs in the cell-culture medium has been measured by raster image correlation spectroscopy (46,72) as $D = (2.1 \pm 0.2)\ \mu m^2/s$ (data not shown), corresponding to a hydrodynamic radius of (106 ± 10) nm and to an average aggregation number of ~3 units.

Cell culture

HeLa cells have been cultured in complete DMEM, 10% FBS at 37°C with 5% CO_2 and have been routinely split 1:10 in culture dishes when at ~80% confluence. The cells have been incubated for 4 h at 37°C up to a final GNSs concentration of 25 μg/mL, which has been proven by previous cell viability tests (14) to be noncytotoxic to cells up to 24 h. For the incubation process, no FBS has been added.

Confocal reflectance microscopy and image correlation spectroscopy

All the *xyt* stacks have been acquired with a model No. SP5 TCS confocal microscope (Leica Microsystems, Wetzlar, Germany). The GNSs scattering signal has been primed by the 488 nm line of an Argon ion laser ($P = 20\ \mu W$) and has been collected in back-scattering geometry by a 40× Plan-Apochromat oil immersion objective (N.A. = 1.3, $\theta = 60°$); a photomultiplier tube has been employed for the signal detection.

Raster-scanned scattered- and transmitted-light images have been acquired simultaneously and the superposition of the first and last frames of both *xyt* stacks has been exploited to exclude the loss of the *z*-focal plane positioning and the occurrence of whole-cell displacements throughout the acquisition. The microscope stage drift has been evaluated by STICS analyses on immobile 0.1-μm fluorescent spheres: no displacement (less than a pixel) has been detected in the STCF peak under the same imaging conditions adopted for the investigation of the GNSs dynamics (data not shown).

Images have been acquired at a 400-Hz line-scan frequency continuously up to 500 frames, on 30–40 μm fields of view. With a 1024 × 1024 resolution, image acquisition time was 2.5 s and the pixel size was 0.03–0.04 μm. For the TICS analysis only, pixels have been rebinned to a final size comparable to the optical PSF (0.2 μm). All the correlation functions have been computed by a custom-written Python code exploiting fast Fourier transform routines, whereas nonlinear curve fitting has been performed by the Origin Pro 8.6 software (OriginLab, Northampton, MA). The zero-lag correlation values have always been excluded from the fitting procedure.

SPT data analysis

SPT has been performed on the same *xyt* stacks analyzed by TICS, STICS, and kICS. The tracking software Imaris (Bitplane, Zurich, Switzerland) has been employed to compute the particle trajectories, which have been analyzed by a custom-written Python code.

RESULTS AND DISCUSSION

Time-lapse confocal reflectance imaging (73) has been performed on GNSs-treated and untreated cells for comparison: in agreement with two-photon excitation experiments, scattered-light images reveal that GNSs are internalized within vesicles (Fig. S1 in the Supporting Material) comparable to or larger than the optical PSF. Their typical diameter of 260 ± 35 nm has been determined by Gaussian fits of the radial intensity profiles on 20 objects.

The light-scattering signal fluctuations are here mainly due to vesicles motions (number fluctuations) whereas coherence effects due to phase fluctuations appear to be negligible. The phase factor of a single sphere ($R = 300$ nm) has been simulated and compared (Fig. S2) to the phase factor of an aggregate made by three smaller spheres ($R = 100$ nm equal to the nanoparticles hydrodynamic radius). The two phase factors are very similar for the range of collection angles of our objective (120–240°). Moreover, raster image correlation spectroscopy measurements performed on zoomed intracellular regions so as to increase the time resolution (1 ms/line, 2 μs/pixel) do not reveal any decay in the autocorrelation function, thus excluding subvesicle motions (74) (data not shown).

TICS analysis

The TICS analysis has been performed by computing in each pixel of the 256 × 256 rebinned images the autocorrelation function of Eq. 1. To avoid the ACF computation in pixels containing the only contribution of background scattering, we applied a threshold (a high-pass filter) on the time-averaged pixel intensities $\langle I(x,y,t)\rangle_t$. A fast visualization of the typical timescale of the transport processes producing scattering fluctuations has been obtained by storing and color-coding, for each pixel, the lag-time where the normalized ACF halves. Large differences are found between treated and untreated cells (Fig. 1, *a* and *b*): long time decays occur in the cytoplasm around the cell nucleus for treated cells (Fig. 1 *a*), whereas shorter times are systematically found for untreated cells (Fig. 1 *b*). The difference is evident from the histograms of the characteristic half-height decay times, plotted in Fig. 1 *c*.

Typical experimental ACFs are shown in Fig. 1 *d*, exemplifying the three processes occurring in GNSs-treated cells. The first is a purely diffusive ACF that can be fit to Eq. 2. The typical decay times of diffusive-like ACFs range from 10 to 50 s, yielding diffusion coefficients in the range $(2–5) \times 10^{-4}\ \mu m^2/s$. The diffusion coefficient is 10^4 smaller than that of the same GNSs in solution, consistently with the GNSs uptake by large vesicles (21). The second kind of ACF is well fit by a diffusion-plus-drift model (Eq. 3). Typical drift speed values ~10^{-2}–10^{-3} μm/s are found, comparable to those reported in a variety of studies of internalization of anticancer drugs (75), lipoplexes (76), polyplexes (77), and lipid/DNA nanoparticles (52). The third kind of ACF time behavior cannot be fitted by either of the previous models. Even a fractional α-exponent in the temporal dependence of the diffusive ACF decay, which is usually introduced to account for anomalous subdiffusion (26), does not lead to a satisfactory fit of the data. The more refined analysis performed by spatio-temporal correlation (shown in the next section) is required.

STICS analysis

The acquired *xyt* stacks can also be analyzed by means of the STICS formalism. The 1024 × 1024 images of the

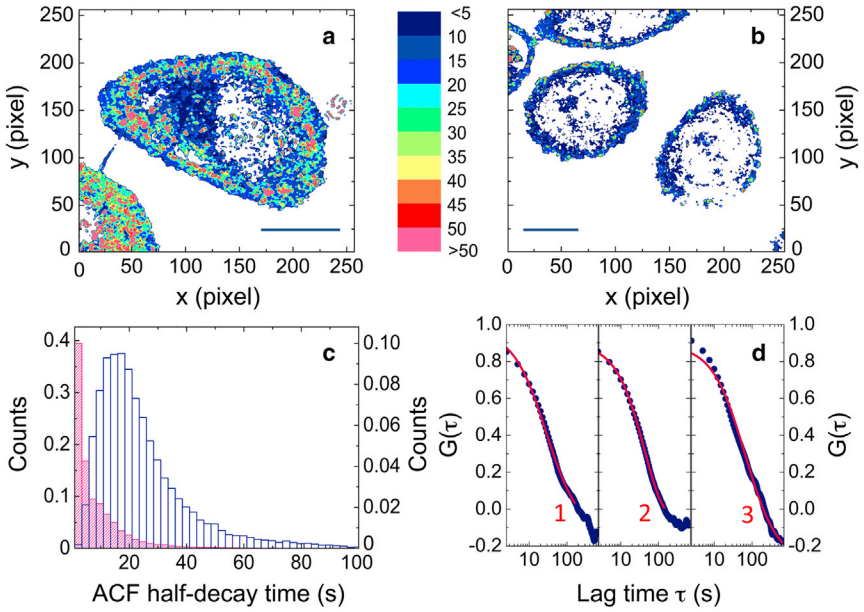

FIGURE 1 TICS analysis. (*a* and *b*) Whole-cell maps of the TICS correlation half-height decay time obtained in GNSs-treated (*a*) and untreated (*b*) HeLa cells; the decay times are color-coded in seconds. The same intensity threshold of 100 a.u. has been applied for the analysis of both *xyt* stacks. In the case of untreated cells, the map has been built from the cellular (vesicles, organelles) background scattering fluctuations. Scale bar = 10 μm in both (*a*) and (*b*). (*c*) Histogram of the correlation half-height decay times recovered from the TICS maps of (*a*) (*open*) and (*b*, *solid*). Each histogram has been normalized to the corresponding total number of counts (excluding the pixels with a time-averaged intensity lower than the applied threshold, shown in *white* in *a* and *b*). (*d*) Exemplifying ACFs recovered on separate 16 × 16 ROIs (2.2 × 2.2 μm) on the *xyt* stack analyzed in (*a*) curve 1, fit to Eq. 2 with $D = (3.6 \pm 0.1) \times 10^{-4}$ μm^2/s; and curve 2, fit to Eq. 3 with $D = (2.21 \pm 0.04) \times 10^{-4}$ μm^2/s and $|\underline{v}| = (3.6 \times 0.1) \times 10^{-3}$ μm/s. Experimental ACFs turn negative at large lag-times and deviate from the theoretical ACF defined in the limit $T \to +\infty$ due to the finite data acquisition and integration time T ($T = 1200$ s, to be compared with the ~50s typical correlation decay time). For curve 3, the best fit to Eq. 3 is shown, evidencing that the ACF cannot be satisfactorily fit by either a diffusion-plus-drift or purely diffusive model. To see this figure in color, go online.

selected cells have been divided in 64 × 64 (2.2 × 2.2 μm) ROIs, the STICS correlation function has been computed on each one according to Eq. 4 and whole-cell maps of the GNSs dynamics have been built from the temporal displacement of the STCFs peak. When more details are required by the particular process examined, a finer grid can be also adopted (78) by a 32 pixels' shift of 64 × 64 ROIs (resulting in a four-times increment of the ROIs examined, here performed on the upper-left quarter of Fig. 2 *a*).

A typical STICS result is exemplified in Fig. 2 *a* for the same cell analyzed by TICS (Fig. 1). Regions of diffusive motions are found (*circles*) together with regions where vesicles exhibit both diffusion and drift (*arrows*) and regions where an anomalous behavior of the STCF is recovered (*squares*). In the four-panel groups of the figure, for the same ROIs already discussed in the TICS analysis (Fig. 1 *d*), STCFs are reported at three different time delays and the ξ- and η-coordinates of the STCF peak $(\xi_{max}, \eta_{max})\delta x$ are plotted versus time. In Fig. 2, *b–e*, the peak of the STCF remains located at the origin of the axes, becoming broader at later times as expected for the diffusive case. Fig. 2, *f–i*, shows the case of a diffusive-plus-drift motion, where the STCF peak coordinates vary linearly with the time delay, allowing the estimate of the modulus and direction of the drift velocity. The direction of the arrows representing the recovered drift velocities in Fig. 2 *a*, indicates that there is not a preferential flux, suggesting that although described by a drift model, the motion of the GNSs collected in large vesicles can be related to transport events in the cytoplasm or along the randomly oriented F-actin filaments. An example of an anomalous behavior is shown in Fig. 2, *j–m*: the peak of the STCF broadens in an asymmetric fashion for increasing lag time values and its position varies nonlinearly with the lag time. A large fraction (40%) of the ROIs shows this behavior. These results do not depend critically on the size of the ROI on which STICS is performed.

To have a more direct insight of the origin of the anomalous, nonlinear trend of the $(\xi_{max}, \eta_{max})\delta x$-versus-$\tau$ plot, we have adopted two approaches: 1) we have performed single particle tracking on selected objects within the cell, and inspected the MSD-versus-τ plot; and 2) we have run numerical simulations to test whether the STCFs obtained starting from assumed models of intracellular transport match the experimental findings.

SPT analysis

SPT has been performed on selected objects providing the trajectory coordinates in the focal plane. As already found by image correlation analyses (TICS and STICS), the experimental MSD curves (examples in Fig. 3 *a*) suggest the existence of different classes of trajectories. MSD 1 reveals a purely diffusive motion (fit to Eq. 13(*i*)); MSD 2 requires the coupling Brownian diffusion-plus-drift motion (fit to Eq. 13(*ii*)); and MSD 3 cannot be fitted by the previous equations, and suggests superdiffusive, subballistic dynamics.

Enhanced diffusion models are found in the literature leading to a $\tau^{3/2}$ power law for the MSD. The 3/2-power dependence has been empirically treated by the introduction of a time-dependent friction coefficient in the generalized Langevin equation (79). An alternative theoretical treatment has been proposed considering motions in a random velocity field (80), which models the effect of the diffusive motion in between two drift (ballistic) events and can be used to model

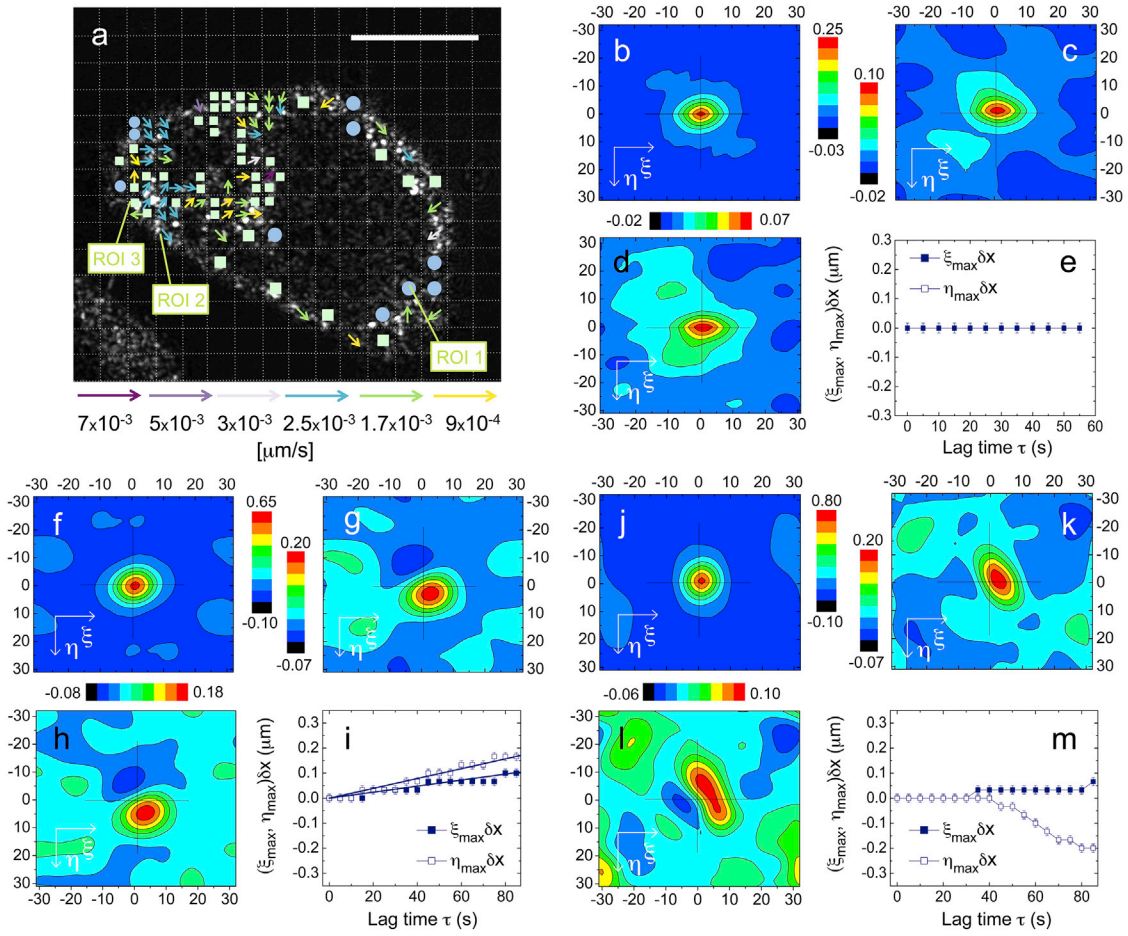

FIGURE 2 STICS analysis. (*a*) STICS map recovered on the same cell analyzed by TICS in Fig. 1, *a* and *d*, classifying the scattering vesicles dynamics in each ROI as purely diffusive (*circles*), diffusive with a drift component (*arrows*, defining the velocity direction and coded according to the speed $|v|$), and anomalous (*squares*); the classification is based on the $(\xi_{max},\eta_{max})\delta x$-versus-$\tau$ plot as described in the text. Two-hundred frames of the raw *xyt* stack have been employed for the computation of the STCFs. Scale bar = 10 μm. (*b–d*) Contour plots of the STICS correlation function $G(\xi,\eta,\tau)$ at fixed lag times ($\tau = 0$ in *b*, 25 s in *c*, and 35 s in *d*) for the ROI identified as 1 in (*a*); the calibration bars code for the correlation amplitude. (*e*) $(\xi_{max},\eta_{max})\delta x$-versus-$\tau$ plot for ROI 1 in (*a*). (*f–h* and *j–l*) Contour plots of the STICS correlation function $G(\xi,\eta,\tau)$ at fixed lag times ($\tau = 0$ s in *f* and *j*, 50 s in *g* and *k*, 75 s in *h* and *l*) for ROIs 2 (*f–h*) and 3 (*j–l*). (*i* and *m*) $(\xi_{max},\eta_{max})\delta x$-versus-$\tau$ plot for ROIs 2 (*i*) and 3 (*m*). For ROI 2, the (ξ_{max},η_{max}) coordinates allow to recover $v_x = (1.20 \pm 0.02) \times 10^{-3}$ μm/s and $v_y = (1.96 \pm 0.03) \times 10^{-3}$ μm/s as best-fit parameters. For (*e*), (*i*), and (*m*), the experimental uncertainty on the STCF peak coordinates is equal to one-half the pixel size. To see this figure in color, go online.

superdiffusion within an intricate network of active filaments (81). However, this model does not lead to an integrable expression to be used in the STICS derivation of the correlation function. The same reasoning applies to the Lévy-walks model (82–85), which is used in the literature to describe enhanced diffusion but lacks to give a finite second moment of the diffusion propagator (probability density of finding a particle at a given distance from the origin at a certain lag time). Again this model leads to a formalism that is not analytically transferable to the STICS framework.

Hypothesizing that cytoskeleton-based transport is responsible for the enhanced diffusion revealed by STICS and SPT data analysis, we have chosen to ascribe the experimental superdiffusive MSD to a sequence of jumps between a purely diffusive Brownian motion regime (passive transport) to an active transport regime (Eq. 6). The advantage of this model is that it stems from derivable and physically meaningful parameters: namely, the diffusion coefficient, the drift velocity, and the transition rates between the passive and the active state. In agreement with this model, the MSD can be fitted to Eq. 13(*iii*), although up to four parameters are needed. The two rates k_{12} and k_{21} describing the intermittent diffusion are especially difficult to extract from the fit of individual MSDs due to the complex multiparameter dependence of the fit function.

A more reliable estimate of all the parameters of the intermittent Brownian diffusion-drift model can be obtained by implementing the Bayesian-based maximum-likelihood analysis described in the Materials and Methods. Fig. 3, *c–h*, shows the outcome of the MCMC algorithm on an exemplary trajectory (Fig. 3 *b*) exhibiting intermittency between diffusion and active transport. In Fig. 3 *c*, the

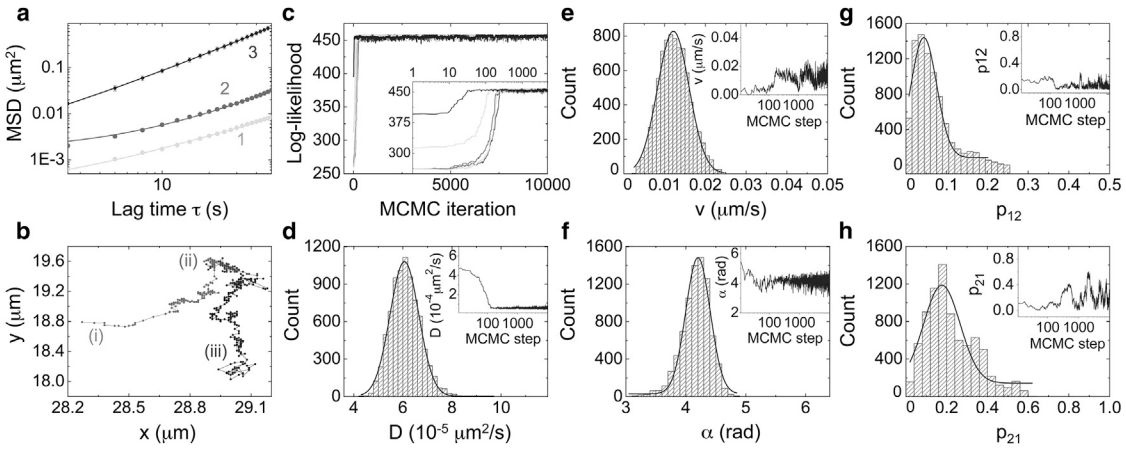

FIGURE 3 MSD-based and Bayesian analysis of single particle tracking data. (*a*) MSD-versus-τ for three trajectories recovered by SPT within the same cell analyzed in Figs. 1 and 2. At each lag time τ, the MSD is reported as mean $\pm$ standard deviation over the whole trajectory length; error bars are within the size of data points. Curve 1, fit to Eq. 13(*i*), with $D = (3.87 \pm 0.05) \times 10^{-5}$ μm^2/s, curve 2 fit to Eq.13(*ii*), with $D = (8.9 \pm 0.3) \times 10^{-5}$ μm^2/s and $|\underline{v}| = (2.26 \pm 0.04) \times 10^{-3}$ μm/s; curve 3 reveals intermittent active transport (fit to Eq. 13(*iii*) with $D = (1.4 \pm 0.1) \times 10^{-3}$ μm^2/s, $|\underline{v}|_{\text{eff}} = (1.12 \pm 0.04) \times 10^{-2}$ μm/s, $\tau_{\text{rel}} = (8 \pm 3)$s and $k_{21}/k_{12} = 2.1 \pm 0.5$). (*b*) SPT trajectory exhibiting intermittency between diffusion and active transport. The Bayesian-based MCMC analysis has been performed separately on segments (*i–iii*): results in (*c–h*) refer to portion (*i*), while results for portions (*ii*) and (*iii*) are reported in Fig. S4. (*c*) Log-likelihood as a function of the MCMC iteration step for five independent runs. (*Inset*) Log-scale, used to magnify the code convergence to the same likelihood global maximum. (*d–h*) Histograms of the parameter values explored during the log-likelihood maximization after the initial convergence steps. Data refer to D, $|\underline{v}|$, α, p_{12}, and p_{21} (*d–h*, respectively). The mean values recovered by the Gaussian fits identify the most probable parameter set $\Theta = \{D = (6.1 \pm 0.6) \times 10^{-5}$ μm^2/s, $|\underline{v}| = (1.2 \pm 0.4) \times 10^{-2}$ μm/s, $\alpha = (241 \pm 12)^\circ$, $p_{12} = 0.04 \pm 0.03$, and $p_{21} = 0.18 \pm 0.09\}$ given the experimental trajectory ($p^{\text{eq}}{}_1 = 0.8 \pm 0.1$). (In the *inset* of each panel, the value proposed for the corresponding parameter as a function of the maximum-likelihood iteration is reported.)

log-likelihood is plotted as a function of the iteration step for five separate MCMC runs on the same intermittent-type trajectory, evidencing the convergence to the likelihood global maximum. Similarly, the trend of the model parameters is reported in the insets of Fig. 3, *d–h*, together with the corresponding histograms obtained once the maximum likelihood code has reached convergence. We remark that the histograms are not to be intended as a distribution of values at the different time steps of the trajectory, being instead the values recovered at each step of the MCMC code for the whole trajectory. The results strongly support that an intermittent model can be adopted to describe the GNSs experimental intracellular trajectories. The same model also includes the single-state full diffusive ($p_{12} = 0$) or diffusive-plus-drift ($p_{21} = 0$) limit behaviors, as shown in Fig. S3, where the MCMC analysis for a purely diffusive trajectory is reported for comparison.

Numerical simulations

Numerical simulations (Note S3 in the Supporting Material) have been employed to assess whether the τ-dependence of the peak coordinates of the STICS correlation functions agrees with the specific assumed transport models. At first, a Monte Carlo simulation with increasing number of objects in the ROI has been performed to test whether the presence of particles exhibiting uniform drift along different directions could lead to the anomalous behavior of the peak position graphs. As shown in Fig. S5, the peak position displacement resembles the one found experimentally, though the MSD remains quadratic versus the lag time as expected in the case of Brownian diffusion-plus-drift. The MSD derived on experimental data, which often deviates from this quadratic dependence, allows therefore excluding the presence of multiple drift velocity directions as the reason of the nonlinear ($\xi_{\max}$, $\eta_{\max}$)δx-versus-τ-plot. Numerical simulations have then been performed according to the intermittent model (Eq. 6): in this case, both the experimental MSDs and the recovered SPT trajectories (Fig. 3) are reproduced by simulations. The intermittent active transport model also reproduces the nonlinear ($\xi_{\max}$, $\eta_{\max}$)δx-versus-τ-plots (Fig. S6).

kICS analysis

SPT analysis with maximum likelihood fitting provides direct insight in what we believe is an appropriate effective dynamic model. However, it is time-consuming, it requires the identification of individual objects inside the cell preventing a ROI-by-ROI analysis, and it depends on the signal/noise. It would be desirable to have a straightforward approach to be applied to the raw images as in STICS.

As shown in the Materials and Methods, the formalism of a two-state intermittent model cannot be used to derive an analytical expression of the STCF in the (x,t)-space. By contrast, an analytical expression of the STCF, $G(\underline{k},\tau)$, can be achieved by operating in the Fourier k-space, thereby exploiting the kICS analysis of Eqs. 9–11.

kICS simulations

$G(k,\tau)$ is effectively a time-series in the complex field, with each frame being the average 2D spatial correlation of the Fourier transforms of pairs of images that are a lag-time-τ apart in the experimental dataset. Two choices are possible for data fitting: either analyzing the $G(\underline{k},\tau)$-versus-τ-profiles at fixed k delays, or fitting the $G(\underline{k},\tau)$-versus-k surfaces at fixed lag time τ. To assess which option gives the better estimate of the parameters (diffusion coefficient D, drift velocity $\underline{v}$, association/dissociation rates k_{12} and k_{21}), we separately investigated the effect of D, $\underline{v}$, and k_{12}, k_{21} (through the two-state system probabilities p_{12} and p_{21}) on simulated kICS correlation functions in both representations, as shown in Fig. 4.

$Re(G(\tau))$ and $Im(G(\tau))$ are reported as functions of the lag time τ for fixed $k = (k_x,k_y) = (-2,0)\mu m^{-1}$ with $D = 2 \times 10^{-4}$ $\mu m^2/s$, $|\underline{v}| = 0.08$ $\mu m/s$ (Fig. 4, *a* and *b*) and $|\underline{v}| = 0.001$ $\mu m/s$ (Fig. 4, *c* and *d*) with an arbitrary direction ($\alpha = 290°$) for the velocity vector. Several probability combinations have been explored: 1) $p_{12} = 0.05$ and $p_{21} = 0.05$, 0.4, 0.8; and 2) $p_{12} = 0.5$ and $p_{21} = 0.05$, 0.2, 0.4 (all the combinations are plotted on each panel with the color-code detailed in the figure caption and different line properties for sake of clarity). These p_{12} and p_{21} values correspond to an equilibrium probability for the active transport state p_2^{eq} (Eq. 14) varying in the range 0.06–0.9. The kICS correlation functions, simulated for all possible intermittent transport modes ranging from nearly diffusive to almost totally active, are significantly sensitive to the p_{12} and p_{21} values, especially at high drift speeds (Fig. 4, *a–d*). The diffusion coefficient also affects the kICS profiles simulated in Fig. 4, *e* and *f*, with D in the range $2 \times 10^{-5} - 2 \times 10^{-3}$ $\mu m^2/s$, $\underline{k} = (-2,0)\mu m^{-1}$, $|\underline{v}| = 0.001$ $\mu m/s$, $\alpha = 290°$, $p_{12} = 0.05$, and $p_{21} = 0.4$.

Although the imaginary part of $G(\tau)$ shows the greater sensitivity to differences in the probability values, we evaluated the possibility of fitting the ratio $Im(G(\tau))/Re(G(\tau))$ (representing the tangent of the phase of $G(\tau)$) in order not to discard the contribution of the real part. However, this function does not guarantee the necessary stability, exhibiting the periodic divergence of a tangent function (Fig. S7). On the other hand, the modulus of $G(\tau)$, being always positive, flattens the behavior of the curves becoming less sensitive to the parameters (Fig. S7). A good compromise is represented by the product $Re(G(\tau))\cdot Im(G(\tau))$, which is related (apart from a factor $2i$) to the double product obtained by squaring $G(\tau)$. As can be seen in Fig. 4, *g* and *h*, this function depends sensibly upon the transition rates of the intermittent model.

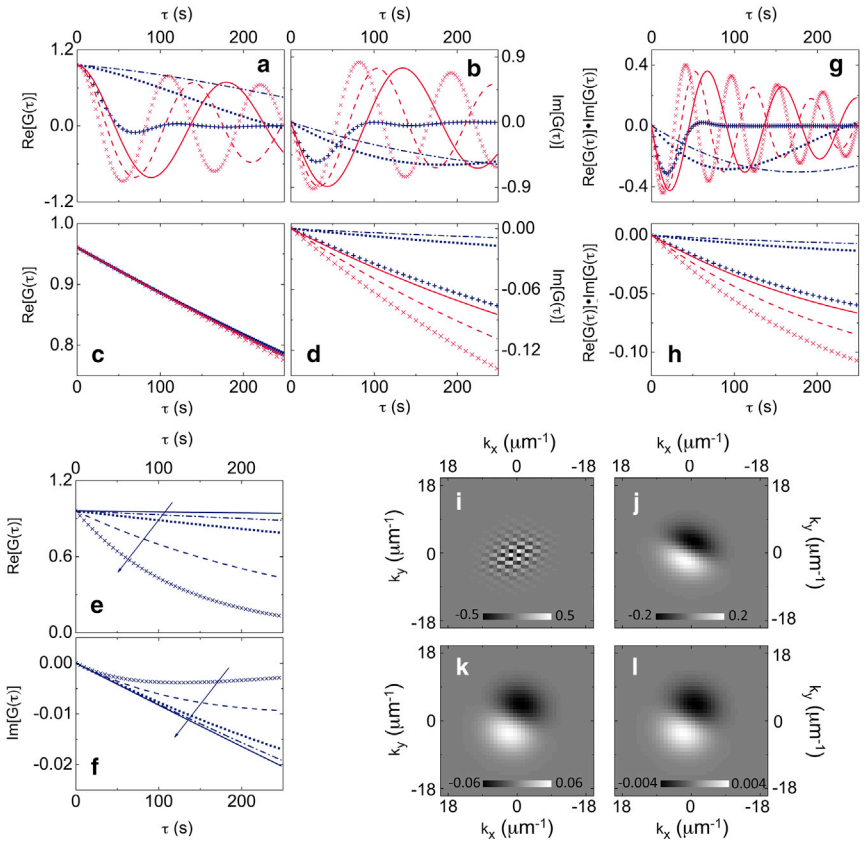

FIGURE 4 Simulated kICS correlation functions. (*a* and *b*) Simulated $Re(G(\tau))$ (in *a*) and $Im(G(\tau))$ (in *b*) profiles for fixed $k = (-2,0)$ μm^{-1}, $D = 2 \times 10^{-4}$ $\mu m^2/s$, and $|\underline{v}| = 0.08$ $\mu m/s$; $p_{12} = 0.05$ for blue curves ($p_{21} = 0.05$, *crosses*; 0.4, *squares*; 0.8, *dashed-dotted*), and $p_{12} = 0.5$ for red curves ($p_{21} = 0.05$, *crosses*; 0.2, *dashed*; 0.4, *solid*). (*c* and *d*) Same simulation parameters and color-code of (*a*) and (*b*) apart from $|\underline{v}| = 0.001$ $\mu m/s$. (*e* and *f*) Simulated $Re(G(\tau))$ (in *e*) and $Im(G(\tau))$ (in *f*) profiles for $D = 2 \times 10^{-5}$, 8×10^{-5}, 2×10^{-4}, 8×10^{-4}, and 2×10^{-3} $\mu m^2/s$ (increasing in the direction of the *arrow*), $|\underline{v}| = 0.001$ $\mu m/s$, $k = (-2,0)\mu m^{-1}$, $p_{12} = 0.05$, and $p_{21} = 0.4$. (*g*) $Re(G(\tau))\cdot Im(G(\tau))$ profiles simulated with the same parameters and color-code of (*a*) and (*b*). (*h*) $Re(G(\tau))\cdot Im(G(\tau))$ profiles simulated with the same parameters and color-code of (*c*) and (*d*). (*i* and *j*) Product of the real and imaginary parts of the $G(k)$ surface simulated for $\tau = 25$ s, $D = 2 \times 10^{-4}$ $\mu m^2/s$, $|\underline{v}| = 0.08$ $\mu m/s$; $\{p_{12} = 0.5, p_{21} = 0.05\}$ in (*i*), $\{p_{12} = 0.05, p_{21} = 0.8\}$ in (*j*). (*k* and *l*) Product of the real and imaginary parts of the $G(k)$ surface simulated for $\tau = 25$ s, $D = 2 \times 10^{-4}$ $\mu m^2/s$, $|\underline{v}| = 0.001$ $\mu m/s$; $\{p_{12} = 0.5, p_{21} = 0.05\}$ in (*k*), $\{p_{12} = 0.05, p_{21} = 0.8\}$ in (*l*). All the simulations have been run on a Python code, which computes the kICS correlation function profiles in the complex field through Eqs. 9–11. The e^{-2} radius of the excitation laser beam and the angle defining the direction of the velocity vector have been kept fixed to $\omega_0 = 0.2$ μm and $\alpha = 290°$ for all the simulations. To see this figure in color, go online.

$Re(G(\underline{k}))\cdot Im(G(\underline{k}))$-versus-$k$ surfaces simulated at fixed lag time ($\tau = 25$ s) are reported in Fig. 4 with $D = 2 \times 10^{-4}$ μm^2/s, $\alpha = 290°$, $|\underline{v}| = 0.08$ μm/s (Fig. 4, *i* and *j*), and $|\underline{v}| = 0.001$ μm/s (Fig. 4, *k* and *l*) for the two extreme values of the p_{12} and p_{21} probabilities combinations previously employed $\{p_{12} = 0.05, p_{21} = 0.8\}$ and $\{p_{12} = 0.5, p_{21} = 0.05\}$). A large difference in the surfaces, leading to a reliable recovery of the probabilities from the $G(\underline{k},\tau)$-versus-$\underline{k}$ 2D surfaces, is obtained for the highest value of the drift velocity, whereas at the lower, the surfaces become more and more insensitive to the probability values (Fig. 4, *k* and *l*).

Fig. 4, *i–l*, also reveals that $Re(G(\underline{k}))\cdot Im(G(\underline{k}))$ surfaces decorrelate, for our typical D and $|\underline{v}|$ values, in the ~0–10 μm^{-1} k-range. When a confocal *xyt* stack is Fourier-transformed, the pixel size and the ROI size (51) determine the obtained k vectors. Therefore, an adequate sampling of ~0–10 μm^{-1} reciprocal-space vectors starting from a 64 × 64 ROI would require a pixel size of ~0.2 μm. This coarse spatial sampling required by $G(\underline{k},\tau)$-versus-$\underline{k}$ surfaces could be obtained on the same experimental dataset analyzed by STICS by pixel rebinning, at the expense of the number of pixels on which the correlation function is averaged. Alternatively the ROI size can be increased, thereby lowering the number of ROIs into which the cell is divided.

By contrast, even a single k vector can be exploited to extract the corresponding $G(\underline{k},\tau)$-versus-τ plot, with the same temporal sampling suitable for STICS. No particular $\underline{k}$ vector has been identified as optimal to this aim. Fig. S8 shows an $Re(G(\underline{k}))\cdot Im(G(\underline{k}))$ surface with several k vectors chosen for the extraction of the corresponding $G(\tau)$ profiles. Apart from amplitude variations, no profile appears preferred. An advantage of $G(\underline{k},\tau)$-versus-$\underline{k}$ surfaces is that they allow the immediate detection of the drift direction, which is orthogonal to the displacement between the positive and the negative lobes (Figs. 4, *i–l*, and S8).

From the above considerations and taking into account the computationally heavier effort in performing surface fitting of a complex function, we suggest to fit the experimental $G(\underline{k},\tau)$-versus-τ plots due to the higher sensitivity toward p_{12} and p_{21} probabilities and the less strict requirements concerning spatial sampling. To increase the precision in the parameters recovery and to decrease the eventual cross correlation among the parameters in the fit, it is convenient to perform a global fit over several $G(\underline{k},\tau)$-versus-τ at different $\underline{k}$ values.

kICS data fitting

Once investigated the effect of D, $|\underline{v}|$, p_{12}, and p_{21} on the kICS correlation function, we employed reciprocal-space correlation spectroscopy for the analysis of the same *xyt* stacks previously examined by STICS. Each 64 × 64 ROI has been Fourier-transformed to yield $G(\underline{k},\tau)$; in the upper-left quarter, a finer grid has been adopted by a 32-pixels shift of the ROIs. Then, $G(\underline{k},\tau)$-versus-τ profiles have been extracted for selected components k_x and k_y and fitted according to Eqs. 9–11. Whole-cell maps have been obtained for each of the parameters derived from the fit: in Fig. 5 *a* the map for p_2^{eq}, recovered on the same cell of Figs. 1 and 2, is shown. D *e* $|\underline{v}|$ maps (Fig. 5, *b* and *c*) highlight the variability of both diffusion coefficients (in the range ~10^{-5}–10^{-3} μm^2/s) and speed values (in the range ~10^{-4}–10^{-2} μm/s). For the three ROIs analyzed by TICS in Fig. 1 *d* and by STICS in Fig. 2, exhibiting Brownian diffusion (ROI 1), Brownian diffusion coupled to directed motion (ROI 2), and intermittent active transport (ROI 3), exemplary $Re(G(\tau))\cdot Im(G(\tau))$ profiles are shown in Fig. 5 *d*. To be noted is that for ROI 1, only $Re(G(\tau))$ is plotted. Best-fit parameters, reported in the caption, are comparable to those obtained by STICS in Fig. 2 for ROI 2. For completeness, the experimental kICS surfaces for the three ROIs at $\tau = 30$ are reported in Fig. S9.

We remark that when the intermittent model is employed to fit $G(\underline{k},\tau)$-versus-τ profiles (such as the one reported for ROI 2) arising from a single-state $D+\underline{v}$ system, transition rates $k_{12}\to+\infty$ and $k_{21}\to 0$ are recovered; similarly, $k_{12}\to 0$, $k_{21}\to+\infty$, and $|\underline{v}|\to 0$ are obtained for a purely diffusive system, thereby confirming that easier transport modes can be easily discriminated and no prior information about the mode of motion is required for the fitting function selection.

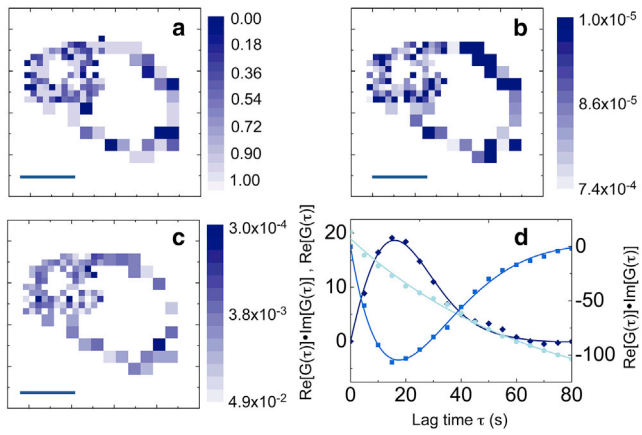

FIGURE 5 kICS analysis. The parameters p_2^{eq} (*a*), D (*b*), and $|\underline{v}|$ (*c*) coded maps obtained by kICS on the same cell analyzed in Figs. 1 and 2. Scale bar = 10 μm. D and $|\underline{v}|$ are coded in μm^2/s and μm/s, respectively. In the upper-left quarter of (*a*)–(*c*), a 32-pixels shift has been adopted to increase the detail in parameters recovery. (*d*) Exemplifying $Re(G(\tau))\cdot Im(G(\tau))$ profiles for ROI 2 ($k_x = 0$, $k_y = -8.9$ μm^{-1}; *right axis*, *squares*) and ROI 3 ($k_x = 0$, $k_y = -11.8$ μm^{-1}; *left axis*, *diamonds*). Best fit parameters are $D = (3.1 \pm 0.3) \times 10^{-4}$ μm^2/s, $|\underline{v}| = (2.47 \pm 0.03) \times 10^{-3}$ μm/s, $\alpha = (59 \pm 1)°$ for ROI 2 (fit to Eq. 12); for ROI 3 (fit to Eqs. 9–11), $D = (7 \pm 4) \times 10^{-5}$ μm^2/s, $|\underline{v}| = (6.1 \pm 0.1) \times 10^{-3}$ μm/s, $\alpha = (295 \pm 2)°$, $k_{12} = (0.007 \pm 0.004)$s^{-1}, and $k_{21} = (0.013 \pm 0.004)$s^{-1}. The $Re(G(\tau))$ plot is shown for ROI 1 ($k_x = -11.8$ μm^{-1}, $k_y = -17.7$ μm^{-1}; *left axis*, *circles*), fitted to Eq. 12 with $|\underline{v}| = 0$ and $D = (3.5 \pm 0.4) \times 10^{-4}$ μm^2/s. Error bars are within the size of data points. To see this figure in color, go online.

Due to the low values of the recovered diffusion coefficient and drift speed, the 2D approximation seems reasonable. The effect of this approximation has been discussed and quantified on an analytically solved case (diffusion plus drift) in Note S4 and Fig. S10 in the Supporting Material.

CONCLUSIONS

We present the theory and the application of a Fourier-space spatio-temporal correlation (kICS) analysis based on an intermittent model that can explain a plethora of intracellular processes leading to measurable parameters such as diffusion coefficient, drift velocity, and on- and off-probabilities between passive and active transport. To further support the model adopted, a particle tracking analysis though a Bayesian code has been implemented. Both methods are able to recover the parameters describing the intermittent model adopted; kICS analysis, however, gives a more routine procedure that is applicable even in those cases when single particle tracking cannot be accomplished due to the poor signal/noise of the images. The protocol has been applied to gold nanoparticles motion in cells detected through their scattering signal, but the same formalism can be applied to fluorescent objects.

SUPPORTING MATERIAL

Supporting Materials and Methods and ten figures are available at http://www.biophysj.org/biophysj/supplemental/S0006-3495(15)01099-1.

AUTHOR CONTRIBUTIONS

M.B. performed the measurements, analyzed the data, derived the theoretical framework, and wrote the article; M.C. supervised the project, analyzed the data, derived the theoretical framework, and wrote the article; G.C. derived the theoretical framework; D.I. provided HeLa cells; P.P. provided gold nanostars; L.S. performed the measurements; and L.D. wrote the article.

ACKNOWLEDGMENTS

We thank Prof. Edoardo Milotti for useful discussion on Bayesian methods.

This work was supported by Academic Funding from The University of Milano-Bicocca (UNIMIB grant a.y. 2014 to M.C.).

SUPPORTING CITATIONS

Reference (86) appears in the Supporting Material.

REFERENCES

1. Link, S., and M. A. El-Sayed. 2000. Shape and size dependence of radiative, non-radiative and photothermal properties of gold nanocrystals. *Int. Rev. Phys. Chem.* 19:409–453.
2. Chou, C. H., C. D. Chen, and C. R. C. Wang. 2005. Highly efficient, wavelength-tunable, gold nanoparticle based optothermal nanoconvertors. *J. Phys. Chem. B.* 109:11135–11138.
3. Hirsch, L. R., R. J. Stafford, …, J. L. West. 2003. Nanoshell-mediated near-infrared thermal therapy of tumors under magnetic resonance guidance. *Proc. Natl. Acad. Sci. USA.* 100:13549–13554.
4. Huang, X., I. H. El-Sayed, …, M. A. El-Sayed. 2006. Cancer cell imaging and photothermal therapy in the near-infrared region by using gold nanorods. *J. Am. Chem. Soc.* 128:2115–2120.
5. Loo, C., A. Lowery, …, R. Drezek. 2005. Immunotargeted nanoshells for integrated cancer imaging and therapy. *Nano Lett.* 5:709–711.
6. Khandelia, R., A. Jaiswal, …, A. Chattopadhyay. 2013. Gold nanoparticle-protein agglomerates as versatile nanocarriers for drug delivery. *Small.* 9:3494–3505.
7. Ghosh, P., G. Han, …, V. M. Rotello. 2008. Gold nanoparticles in delivery applications. *Adv. Drug Deliv. Rev.* 60:1307–1315.
8. Li, N., P. Zhao, and D. Astruc. 2014. Anisotropic gold nanoparticles: synthesis, properties, applications, and toxicity. *Angew. Chem. Int. Ed. Engl.* 53:1756–1789.
9. Guerrero-Martínez, A., S. Barbosa, …, L. M. Liz-Marzán. 2011. Nanostars shine bright for you: colloidal synthesis, properties and applications of branched metallic nanoparticles. *Curr. Opin. Colloid Interface Sci.* 16:118–127.
10. Skrabalak, S. E., J. Chen, …, Y. Xia. 2007. Gold nanocages for biomedical applications. *Adv. Mater.* 19:3177–3184.
11. Eustis, S., and M. A. el-Sayed. 2006. Why gold nanoparticles are more precious than pretty gold: noble metal surface plasmon resonance and its enhancement of the radiative and nonradiative properties of nanocrystals of different shapes. *Chem. Soc. Rev.* 35:209–217.
12. Jain, P. K., K. S. Lee, …, M. A. El-Sayed. 2006. Calculated absorption and scattering properties of gold nanoparticles of different size, shape, and composition: applications in biological imaging and biomedicine. *J. Phys. Chem. B.* 110:7238–7248.
13. Pallavicini, P., G. Chirico, …, A. Taglietti. 2011. Synthesis of branched Au nanoparticles with tunable near-infrared LSPR using a zwitterionic surfactant. *Chem. Commun. (Camb.).* 47:1315–1317.
14. Sironi, L., S. Freddi, …, G. Chirico. 2012. Gold branched nanoparticles for cellular treatments. *J. Phys. Chem. C.* 116:18407–18418.
15. Tong, L., Q. Wei, …, J. X. Cheng. 2009. Gold nanorods as contrast agents for biological imaging: optical properties, surface conjugation and photothermal effects. *Photochem. Photobiol.* 85:21–32.
16. Wang, H., T. B. Huff, …, J. X. Cheng. 2005. In vitro and in vivo two-photon luminescence imaging of single gold nanorods. *Proc. Natl. Acad. Sci. USA.* 102:15752–15756.
17. Verma, A., and F. Stellacci. 2010. Effect of surface properties on nanoparticle-cell interactions. *Small.* 6:12–21.
18. Petros, R. A., and J. M. DeSimone. 2010. Strategies in the design of nanoparticles for therapeutic applications. *Nat. Rev. Drug Discov.* 9:615–627.
19. Chithrani, B. D., A. A. Ghazani, and W. C. W. Chan. 2006. Determining the size and shape dependence of gold nanoparticle uptake into mammalian cells. *Nano Lett.* 6:662–668.
20. Hemmerich, P. H., and A. H. von Mikecz. 2013. Defining the subcellular interface of nanoparticles by live-cell imaging. *PLoS One.* 8: e62018.
21. van den Broek, B., B. Ashcroft, …, J. van Noort. 2013. Parallel nanometric 3D tracking of intracellular gold nanorods using multifocal two-photon microscopy. *Nano Lett.* 13:980–986.
22. Arcizet, D., B. Meier, …, D. Heinrich. 2008. Temporal analysis of active and passive transport in living cells. *Phys. Rev. Lett.* 101:248103.
23. Bruno, L., V. Levi, …, M. A. Despósito. 2009. Transition to superdiffusive behavior in intracellular actin-based transport mediated by molecular motors. *Phys. Rev. E Stat. Nonlin. Soft Matter Phys.* 80:011912.

24. Weiss, M., M. Elsner, …, T. Nilsson. 2004. Anomalous subdiffusion is a measure for cytoplasmic crowding in living cells. *Biophys. J.* 87:3518–3524.

25. Guigas, G., C. Kalla, and M. Weiss. 2007. Probing the nanoscale viscoelasticity of intracellular fluids in living cells. *Biophys. J.* 93:316–323.

26. Wu, J., and K. M. Berland. 2008. Propagators and time-dependent diffusion coefficients for anomalous diffusion. *Biophys. J.* 95:2049–2052.

27. Mallik, R., and S. P. Gross. 2004. Molecular motors: strategies to get along. *Curr. Biol.* 14:R971–R982.

28. Suh, J., D. Wirtz, and J. Hanes. 2003. Efficient active transport of gene nanocarriers to the cell nucleus. *Proc. Natl. Acad. Sci. USA.* 100:3878–3882.

29. Huefner, A., D. Septiadi, …, S. Mahajan. 2014. Gold nanoparticles explore cells: cellular uptake and their use as intracellular probes. *Methods.* 68:354–363.

30. Hess, H., and Y. Tseng. 2007. Active intracellular transport of nanoparticles: opportunity or threat? *ACS Nano.* 1:390–392.

31. Tong, L., Y. Zhao, …, J. X. Cheng. 2007. Gold nanorods mediate tumor cell death by compromising membrane integrity. *Adv. Mater.* 19:3136–3141.

32. Loverdo, C., O. Bénichou, …, R. Voituriez. 2008. Enhanced reaction kinetics in biological cells. *Nat. Phys.* 4:134–137.

33. Bénichou, O., C. Loverdo, …, R. Voituriez. 2006. Two-dimensional intermittent search processes: an alternative to Lévy flight strategies. *Phys. Rev. E Stat. Nonlin. Soft Matter Phys.* 74:020102, (R).

34. Bénichou, O., C. Loverdo, …, R. Voituriez. 2007. A minimal model of intermittent search in dimension two. *J. Phys. Condens. Matter.* 19:065141.

35. Elson, E. L., and D. Magde. 1974. Fluorescence correlation spectroscopy. I. Conceptual basis and theory. *Biopolymers.* 13:1–27.

36. Magde, D., E. L. Elson, and W. W. Webb. 1974. Fluorescence correlation spectroscopy. II. An experimental realization. *Biopolymers.* 13:29–61.

37. Wiseman, P. W., J. A. Squier, …, K. R. Wilson. 2000. Two-photon image correlation spectroscopy and image cross-correlation spectroscopy. *J. Microsc.* 200:14–25.

38. Kolin, D. L., S. Costantino, and P. W. Wiseman. 2006. Sampling effects, noise, and photobleaching in temporal image correlation spectroscopy. *Biophys. J.* 90:628–639.

39. Elson, E. L. 2011. Fluorescence correlation spectroscopy: past, present, future. *Biophys. J.* 101:2855–2870.

40. Schwille, P. 2001. Fluorescence correlation spectroscopy and its potential for intracellular applications. *Cell Biochem. Biophys.* 34:383–408.

41. Hebert, B., S. Costantino, and P. W. Wiseman. 2005. Spatiotemporal image correlation spectroscopy (STICS) theory, verification, and application to protein velocity mapping in living CHO cells. *Biophys. J.* 88:3601–3614.

42. Yeung, C., M. Shtrahman, and X. L. Wu. 2007. Stick-and-diffuse and caged diffusion: a comparison of two models of synaptic vesicle dynamics. *Biophys. J.* 92:2271–2280.

43. Saffarian, S., and E. L. Elson. 2003. Statistical analysis of fluorescence correlation spectroscopy: the standard deviation and bias. *Biophys. J.* 84:2030–2042.

44. Coppola, S., D. Pozzi, …, G. Caracciolo. 2013. Quantitative measurement of intracellular transport of nanocarriers by spatio-temporal image correlation spectroscopy. *Methods Appl. Fluoresc.* 1:015005.

45. Wiseman, P. W., C. M. Brown, …, A. F. Horwitz. 2004. Spatial mapping of integrin interactions and dynamics during cell migration by image correlation microscopy. *J. Cell Sci.* 117:5521–5534.

46. Digman, M. A., C. M. Brown, …, E. Gratton. 2005. Measuring fast dynamics in solutions and cells with a laser scanning microscope. *Biophys. J.* 89:1317–1327.

47. Potvin-Trottier, L., L. Chen, …, P. W. Wiseman. 2013. A nu-space for image correlation spectroscopy: characterization and application to measure protein transport in live cells. *New J. Phys.* 15:085006.

48. Michelman-Ribeiro, A., D. Mazza, …, J. G. McNally. 2009. Direct measurement of association and dissociation rates of DNA binding in live cells by fluorescence correlation spectroscopy. *Biophys. J.* 97:337–346.

49. Brandão, H. B., H. Sangji, …, P. W. Wiseman. 2014. Measuring ligand-receptor binding kinetics and dynamics using k-space image correlation spectroscopy. *Methods.* 66:273–282.

50. Kolin, D. L., D. Ronis, and P. W. Wiseman. 2006. K-space image correlation spectroscopy: a method for accurate transport measurements independent of fluorophore photophysics. *Biophys. J.* 91:3061–3075.

51. Wiseman, P. W. 2013. Image correlation spectroscopy: mapping correlations in space, time, and reciprocal space. *Methods Enzymol.* 518:245–267.

52. Coppola, S., G. Caracciolo, and T. Schmidt. 2014. Exact occupation probabilities for intermittent transport and application to image correlation spectroscopy. *New J. Phys.* 16:113057.

53. Semrau, S., and T. Schmidt. 2007. Particle image correlation spectroscopy (PICS): retrieving nanometer-scale correlations from high-density single-molecule position data. *Biophys. J.* 92:613–621.

54. Krichevsky, O., and G. Bonnet. 2002. Fluorescence correlation spectroscopy: the technique and its applications. *Rep. Prog. Phys.* 65: 251–297.

55. Schwille, P., F. J. Meyer-Almes, and R. Rigler. 1997. Dual-color fluorescence cross-correlation spectroscopy for multicomponent diffusional analysis in solution. *Biophys. J.* 72:1878–1886.

56. Qian, H., M. P. Sheetz, and E. L. Elson. 1991. Single particle tracking. Analysis of diffusion and flow in two-dimensional systems. *Biophys. J.* 60:910–921.

57. Saxton, M. J., and K. Jacobson. 1997. Single-particle tracking: applications to membrane dynamics. *Annu. Rev. Biophys. Biomol. Struct.* 26: 373–399.

58. Levi, V., and E. Gratton. 2007. Exploring dynamics in living cells by tracking single particles. *Cell Biochem. Biophys.* 48:1–15.

59. Jin, S., and A. S. Verkman. 2007. Single particle tracking of complex diffusion in membranes: simulation and detection of barrier, raft, and interaction phenomena. *J. Phys. Chem. B.* 111:3625–3632.

60. Gal, N., D. Lechtman-Goldstein, and D. Weihs. 2013. Particle tracking in living cells: a review of the mean square displacement method and beyond. *Rheol. Acta.* 52:425–443.

61. Michalet, X. 2010. Mean square displacement analysis of single-particle trajectories with localization error: Brownian motion in an isotropic medium. *Phys. Rev. E Stat. Nonlin. Soft Matter Phys.* 82:041914.

62. Ruthardt, N., D. C. Lamb, and C. Bräuchle. 2011. Single-particle tracking as a quantitative microscopy-based approach to unravel cell entry mechanisms of viruses and pharmaceutical nanoparticles. *Mol. Ther.* 19:1199–1211.

63. Berezhkovskii, A. M., and S. M. Bezrukov. 2011. Effective drift and diffusion of a particle jumping between mobile and immobile states. *J. Electroanal. Chem. (Lausanne).* 660:352–355.

64. Martin, D. S., M. B. Forstner, and J. A. Käs. 2002. Apparent subdiffusion inherent to single particle tracking. *Biophys. J.* 83:2109–2117.

65. Das, R., C. W. Cairo, and D. Coombs. 2009. A hidden Markov model for single particle tracks quantifies dynamic interactions between LFA-1 and the actin cytoskeleton. *PLOS Comput. Biol.* 5:e1000556.

66. Monnier, N., Z. Barry, …, M. Bathe. 2015. Inferring transient particle transport dynamics in live cells. *Nat. Methods.* 12:838–840.

67. Röding, M., M. Guo, …, A. Särkkä. 2014. Identifying directional persistence in intracellular particle motion using hidden Markov models. *Math. Biosci.* 248:140–145.

68. Press, W. H., S. A. Teukolsky, …, B. P. Flannery. 2007. Numerical Recipes: the Art of Scientific Computing, 3rd Ed. Cambridge University Press, Cambridge, UK.

69. Chandrasekhar, S. 1943. Stochastic problem in physics and astronomy. *Rev. Mod. Phys.* 15:1–89.

70. Gilks, W. R., S. Richardson, and D. J. Spiegelhalter. 1995. Markov Chain Monte Carlo in Practice. Chapman & Hall/CRC, London, UK.

71. Casu, A., E. Cabrini, …, P. Pallavicini. 2012. Controlled synthesis of gold nanostars by using a zwitterionic surfactant. *Chemistry.* 18:9381–9390.

72. Brown, C. M., R. B. Dalal, …, E. Gratton. 2008. Raster image correlation spectroscopy (RICS) for measuring fast protein dynamics and concentrations with a commercial laser scanning confocal microscope. *J. Microsc.* 229:78–91.

73. Boustany, N. N., S. A. Boppart, and V. Backman. 2010. Microscopic imaging and spectroscopy with scattered light. *Annu. Rev. Biomed. Eng.* 12:285–314.

74. Toplak, T., E. Pandzic, …, P. W. Wiseman. 2012. STICCS reveals matrix-dependent adhesion slipping and gripping in migrating cells. *Biophys. J.* 103:1672–1682.

75. Penjweini, R., N. Smisdom, …, M. Ameloot. 2014. Transport and accumulation of PVP-Hypericin in cancer and normal cells characterized by image correlation spectroscopy techniques. *Biochim. Biophys. Acta.* 1843:855–865.

76. Coppola, S., L. C. Estrada, …, G. Caracciolo. 2012. Intracellular trafficking of cationic liposome-DNA complexes in living cells. *Soft Matter.* 8:7919–7927.

77. Kulkarni, R. P., D. D. Wu, …, S. E. Fraser. 2005. Quantitating intracellular transport of polyplexes by spatio-temporal image correlation spectroscopy. *Proc. Natl. Acad. Sci. USA.* 102:7523–7528.

78. Pandzic, E., J. Rossy, and K. Gaus. 2015. Tracking molecular dynamics without tracking: image correlation of photo-activation microscopy. *Methods Appl. Fluoresc.* 3:014006.

79. Caspi, A., R. Granek, and M. Elbaum. 2000. Enhanced diffusion in active intracellular transport. *Phys. Rev. Lett.* 85:5655–5658.

80. Zumofen, G., J. Klafter, and A. Blumen. 1990. Enhanced diffusion in random velocity fields. *Phys. Rev. A.* 42:4601–4608.

81. Ajdari, A. 1995. Transport by active filaments. *Europhys. Lett.* 31: 69–74.

82. Bouchaud, J. P., and A. Georges. 1990. Anomalous diffusion in disordered media: statistical mechanisms, models and physical applications. *Phys. Rep.* 195:127–293.

83. Klafter, J., M. F. Shlesinger, and G. Zumofen. 1996. Beyond Brownian motion. *Phys. Today.* 49:33–39.

84. Metzler, R., and J. Klafter. 2004. The restaurant at the end of the random walk: recent developments in the description of anomalous transport by fractional dynamics. *J. Phys. Math. Gen.* 37:R161–R208.

85. Klafter, J., A. Blumen, …, M. F. Shlesinger. 1990. Lévy walk approach to anomalous diffusion. *Physica A.* 168:637–645.

86. Costantino, S., J. W. D. Comeau, …, P. W. Wiseman. 2005. Accuracy and dynamic range of spatial image correlation and cross-correlation spectroscopy. *Biophys. J.* 89:1251–1260.